

## Investigating the hot gas in active Brightest Cluster Galaxies\*

---

A.L. Ratsimbazafy<sup>†1</sup>, S.I. Loubser<sup>1</sup>, M. Donahue<sup>2</sup>, G.M. Voit<sup>2</sup>

<sup>1</sup>Centre for Space Research, North-West University, Potchefstroom 2520, SA

<sup>2</sup>Michigan State University, Physics & Astronomy Department, East Lansing, MI 48824-2320, USA

E-mail: [Ando.Ratsimbazafy@nwu.ac.za](mailto:Ando.Ratsimbazafy@nwu.ac.za), [Ilani.Loubser@nwu.ac.za](mailto:Ilani.Loubser@nwu.ac.za), [donahue@pa.msu.edu](mailto:donahue@pa.msu.edu), [voit@pa.msu.edu](mailto:voit@pa.msu.edu)

We investigate a crucial phase in the cooling–feedback cycle in the star forming Brightest Cluster Galaxies (BCGs) by looking at the optical emission line properties of the reheated gas that ultimately causes the cycle to repeat. We investigate the source, or the mixture of sources, of ionization of the gas. To identify the dominant ionization processes, excitation sources, morphology and kinematics of the hot gas, line ratios over the entire optical wavelength range are necessary. For this purpose, the spatially–resolved spectra over the entire optical wavelength range for eight nearby, active BCGs in X–ray luminous groups and clusters have been obtained with the Southern African Large Telescope (SALT). The BCG sample was chosen to have H $\alpha$  detections – a strong indication of star formation activity, as well as existing hot cluster data from X–ray regime available. The fundamental gas properties such as electron density, gas temperature, metallicity and several abundances were derived using the spectral features across the long wavelength range. The present optical data will be combined with the other multi–wavelength data to form a complete view of the different phases (hot and cold gas and young stars) and how they interact in the processes of star formation and feedback detected in central galaxies in cooling flow systems, as well as the influence of the surrounding intracluster medium (ICM). Here we present our preliminary results on one of those eight BCGs, Hydra A, which shows the complexity and spatial variation of the ionization mechanisms in the nucleus.

*Frontier Research in Astrophysics - II*

23-28 May 2016

Mondello (Palermo), Italy

---

\*based on observations made with the Southern African Large Telescope (SALT)

<sup>†</sup>Speaker.

## 1. Introduction

The most massive and centrally dominant early-type galaxies, referred to as Brightest Cluster Galaxies (BCGs), are often found in the heart of clusters. They dominate over the other cluster members in terms of luminosities and sizes, and often have diffuse extended stellar haloes. A small, but nevertheless non-negligible fraction of these galaxies are very active. This challenges our view of most massive early-type galaxies in clusters which are believed to be “red and dead”. Moreover, BCGs, especially those sitting at the centres of cool-core clusters show signs of activity, such as the presence of a small fraction of young stars [1, 2], radio sources [3], emission-line nebulae [4], excess UV light [5], far-infrared emission from warm dust [6], and molecular hydrogen [7]. A variety of star formation histories have been also found in BCGs located in the centres of X-ray luminous clusters (e.g. in Ref [8]).

In the centre of the cool-core clusters, the hot intracluster gas is dense enough that it should cool quickly and form stars. The X-ray observations revealed that the cooling flows are in reality much smaller than predicted. This has been popularly referred to as the “cooling flow problem”. The central cluster galaxies often host radio-loud AGN which may account for the necessary heating to counteract radiative cooling [9]. Other mechanisms have also been proposed to explain where the hot gas obtains energy: fast shocks [10], self-irradiation by the cooling hot gas [11], turbulent mixing layers etc. The dense core of a galaxy cluster represents a unique environment where the hot ICM is cooling most rapidly, feedback from the AGN is most effective, and the BCG dominates the mass. This represents one of the few places in the Universe where large-scale cooling and feedback processes can be readily observed.

Great progress has been made by theorists and simulators to reproduce the observed properties of these unique objects [12, 13, 14, 15, 16]. Recently, gas accretion models in the centres of clusters have gained impetus. For example, the “cold-gas accretion model” has been used to interpret various observed properties of elliptical galaxies as well as BCGs in the centres of clusters [8, 12].

Multi-wavelength data will form the complete view of the different phases in the star formation and feedback process, from radio to X-ray wavelengths. This project is concerned with the optical emission line properties of the (re)heated gas that ultimately causes the cooling-feedback cycle to repeat. The heating source(s) in BCGs currently remains uncertain as no single heating mechanism reproduces all the emission-line properties within the optical wavelength ranges previously observed. The same dominant mechanism may not apply to all BCG nebulae, and there may be a mixture of heating mechanisms acting within a single nebula [17]. Thus to get more information, which will enable the dominant mechanism(s) to be identified, we measured line ratios over the entire optical wavelength range.

## 2. Observations and Data reduction

Our sample of eight targets has been selected from the literature to have confirmed  $H\alpha$  detections and strong indications of star formation activity [18] and was subsequently observed with the SALT telescope. Where possible, the SALT data were supplemented with existing long-slit data from Gemini/GMOS. The SALT data was obtained with the Robert Stobie Spectrograph (RSS) using PG0900 grating, with a 1.5" slit. The B600 grating was used on Gemini with two different

$\alpha_{J2000}$		09h18m05.7s
$\delta_{J2000}$		-12d05m44s
$z$		0.055
$E(B-V)_{gal}$	(mag)	0.042
Exp. time with SALT	(seconds)	7317 R
Pixel scale with SALT	(arcsec/pix)	0.12
Resolution with SALT	(Å/pix)	0.95
Exp. time with Gemini	(seconds)	3600 B
Pixel scale with Gemini	(arcsec/pix)	0.14
Resolution with Gemini	(Å/pix)	0.91

Table 1: Hydra A properties, and the details of the long-slit observations with SALT and Gemini telescopes. The rest-frame coverage is  $\sim 3500\text{--}5800\text{ \AA}$  for the blue (B) and  $\sim 5000\text{--}7500\text{ \AA}$  for the red (R).



Figure 1: The composite image of Hydra A: the hot gas in blue was observed by Chandra, jets of radio emission in pink by VLA, and the optical image by the Canada–France–Hawaii telescope/DSS. Credit from <http://chandra.harvard.edu/>.

central wavelength settings: 461 and 466 nm with a slit width of 0.75". The slit was placed on the galaxy's major axis. The properties of Hydra A and the details of the long-slit observations with SALT and Gemini telescopes are given in Table 1. Figure 1 illustrates the composite image (10 x 10 arcmin) of Hydra A. Optical image was obtained by the Canada–France–Hawaii telescope, the X-ray image was observed by Chandra and the radio emission was observed by the Very Large Telescope (VLA). This shows the evidence that this galaxy is very active.

The details of the SALT data reduction are given in [19]. The basic Gemini data reductions, which are similar to the SALT reduction, were performed with the Gemini-specific GMOS data reduction package implemented in the standard IRAF package. The spectra were binned so that each spatial bin in the red frame had a minimum signal-to-noise ratio (S/N) of 30. The same bins were then extracted from the blue frames to ensure identical spatial locations of the bins in the blue and red frame. This delivered a minimum S/N ratio of 20 in the blue bins. The same spatial bins were extracted in both the SALT and Gemini data, by taking the difference in pixel scales into account.

### 3. Emission line analysis

#### 3.1 Emission line fitting and internal extinction

The emission lines and absorption lines were fitted simultaneously by adapting the fitting code GANDALF [20]. All 985 stars of the MILES stellar library were used as stellar templates. This stellar library covers a large stellar parameter space which enables to give a very accurate fit of the stellar continuum. The stellar and galaxy spectral resolution and sampling were matched, and the measurements were corrected for instrumental and internal broadening. GANDALF allows users to choose between a reddening law or a multiplicative polynomial to adjust the stellar continuum to

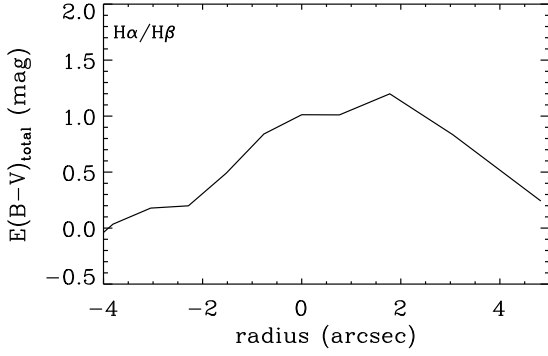


Figure 2: The total derived colour excess in the centre of Hydra A from using  $H\alpha/H\beta$  ratio. These values were used to correct for dust extinction in both blue and red spectra.

fit the overall shape of the observed spectrum. We chose a multiplicative polynomial for this. A high degree of the multiplicative polynomial of 16 was used in order to detect the most weakest lines. GANDALF code accurately separates the stellar continuum and absorption lines from the ionized gas emission. First, the emission line regions were masked, and it fits the spectrum using a set of best-fitting stellar templates in the library. The emission line mask is then lifted and with the stellar kinematics fixed, it reassesses the stellar continuum by simultaneously fitting a number of Gaussian emission-line templates consisting of recombination and forbidden lines.

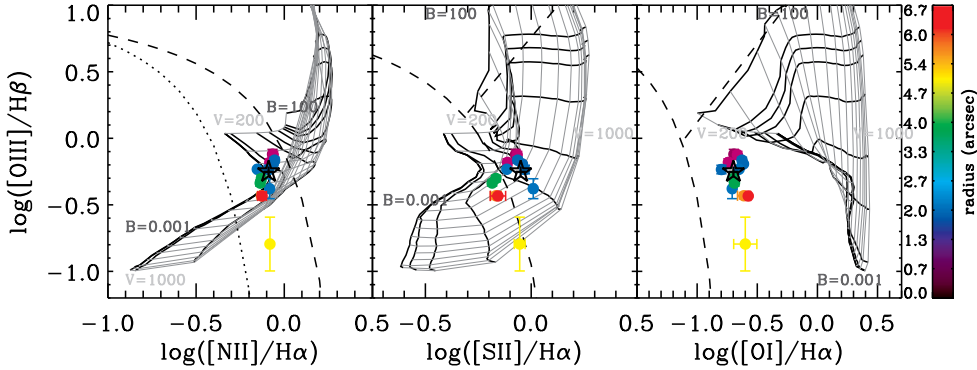


Figure 3: BPT diagrams based on  $[N\ II]\lambda 6584/H\alpha$  (left),  $[S\ II]\lambda\lambda 6717,6731/H\alpha$  (middle) and  $[O\ I]\lambda 6300/H\alpha$  (right). The black star indicates the measurement across the whole galaxy (one large extracted aperture). The demarcation by the dashed and dotted lines separates  $H\ II$  regions, composites and AGN as defined by Kewley et al. [23] and Kauffmann et al. [24] respectively (see text). The model predictions for ionization by shocks are indicated by the grids. These model predictions are from [27] with solar metallicity, pre-shock magnetic fields  $B$  from 0.001 to 100 (dark grey lines), shock velocity of  $V$  from 200 to 1000  $\text{km s}^{-1}$  (light grey lines, slow to fast shocks: from left to right for  $[S\ II]$  and  $[O\ I]$  diagrams, and from top to bottom for  $[N\ II]$ ) and the density  $n_e$  of  $100\ \text{cm}^{-3}$ .

Using the observed Balmer lines ( $H\beta$  and  $H\alpha$ ) in the red spectra<sup>1</sup>, we could estimate the

<sup>1</sup> $H\beta$  and  $H\gamma$  relative strength ratio in the blue frames could also have been used but it is weaker than the Balmer lines in the red frames.

amount of the dust reddening affecting the nebular emission of Hydra A by applying the standard definition of the colour excess. The theoretical flux ratio is  $I(\text{H}\alpha/\text{H}\beta) = 2.86$  for case B recombination ( $n_e 100 \text{ cm}^{-3}$ , and  $T_e 10\,000 \text{ K}$ ). We chose  $R_V$  of 3.1 for this system since Hydra A is a very active galaxy (see Figure 1). We adopted the dust model of Calzetti et al. (2000) [21] to measure the flux attenuation values at the desired wavelength for any given  $E(\text{B}-\text{V})$  value. The total colour excess for the extinction for Hydra A is presented in Figure 2. This  $E(\text{B}-\text{V})$  profile was used to correct both blue and red spectra.

### 3.2 Diagnostic diagrams

Standard diagnostic diagrams e.g. BPT [22] rely on the line ratios  $I([\text{O III}]\lambda 5007)/I(\text{H}\beta)$  versus  $I([\text{N II}]\lambda 6584)/I(\text{H}\alpha)$ ,  $I([\text{S II}]\lambda\lambda 6717, 6731)/I(\text{H}\alpha)$  or  $I([\text{O I}]\lambda 6300)/I(\text{H}\alpha)$ . These diagrams can be constructed for galaxies with optical emission lines to separate ionization from AGN and star formation. Kewley et al. [23] used a combination of photoionization and stellar population synthesis models to place a theoretical upper limit on the location of star forming galaxies ( $\text{H II}$  regions) on the BPT diagram. Thus, the galaxies above the Kewley’s criterion are defined as purely AGN. The AGN branch is generally associated with two populations of sources: the LINERs (low ionization emission) and Seyferts (high ionization emission) regions. Kauffmann et al. [24] revised the Kewley’s criterion to a curve below which represents the  $\text{H II}$  regions. Thus, the area between the two curves contain the composite objects.

We show three BPT diagrams for Hydra A in Figure 3. Different exposures were added, taken in different conditions (notably seeing). This can account for a maximum of  $\sim 1$  arcsec spread in the data points, nevertheless, a clear trend can be seen as the bins are located further from the nucleus of the galaxy. The centre of the galaxy shows LINER-like line ratio whereas the whole galaxy, i.e. if a single large aperture is extracted, is classified as composite by looking at the  $[\text{N II}]/\text{H}\alpha$  diagram. It is important to note that “AGN-like” line ratios can also be caused by other heating mechanisms, and the ionization regions require more detailed modelling to disentangle the complex combination of AGN feedback, shocks, photoionization from hot stars, and other mechanisms.

Heckman et al. [25] have studied dynamical, physical and chemical properties of emission nebulae in different BCGs including Hydra A. They found values of  $\log([\text{N II}]/\text{H}\alpha)$  between  $-0.12$  and  $0.05$  which are in good agreement with our values (see Figure 3),  $\log([\text{S II}]/\text{H}\alpha)$  between  $-0.45$  and  $-0.25$  which are slightly lower than our values, and  $\log([\text{O I}]/\text{H}\alpha)$  between  $-0.60$  and  $-0.42$  which are marginally higher than our values.

### 3.3 Electron density and temperature

The most common means of estimating the hot gas electron density and temperature uses two emission lines of the same element which have different thresholds for collisional excitation. Doublet line ratios such as  $I([\text{S II}]\lambda 6716)/I([\text{S II}]\lambda 6731)$  are very useful measures of electron density in a low-ionization scenario. The density,  $n_e$ , is very weakly dependent on electron temperature. The density equation is iteratively solved using a technique originally developed by [26], applied with the NEBULAR package in STSDAS, layered on the IRAF environment. We show the distribution of the  $[\text{S II}]$  line ratios for the density in Figure 4. The line-emitting gas in the nucleus (marked by the dashed line in the plot) has densities between  $300$  and  $500 \text{ cm}^{-3}$  (assuming  $T_e \sim 10\,000 \text{ K}$ ).

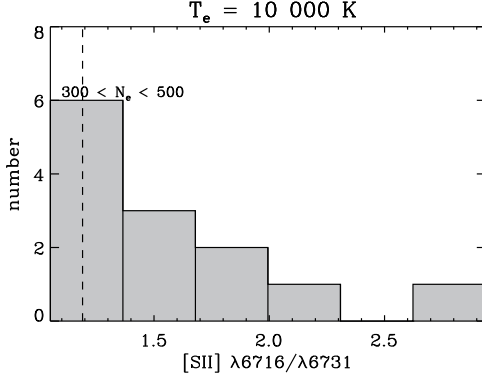


Figure 4: Distribution of the line ratios for density. The density of the gas in the centre of the galaxy is highlighted by the vertical dashed line. The total number of bins measured is 13.

The electron temperature can similarly be measured from the  $I([\text{S II}]\lambda 4068 + [\text{S II}]\lambda 4076)/I([\text{S II}]\lambda 6716 + [\text{S II}]\lambda 6730)$  or  $I([\text{O III}]\lambda 4959 + [\text{O III}]\lambda 5007)/I([\text{O III}]\lambda 4363)$  ratios (depending on the ionization scenario), and is also very weakly dependent on electron density.

### 3.4 Oxygen lines and shocks

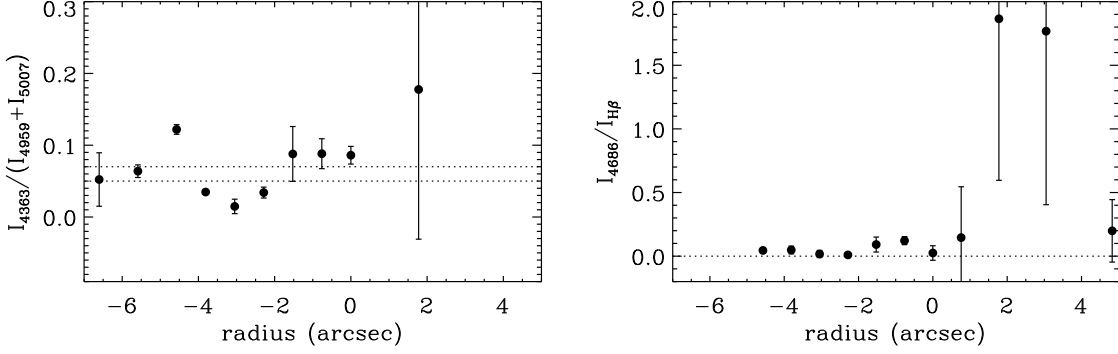
The  $[\text{O III}]\lambda 4363$  line can be used as an indicator for shocks. Measurements of  $[\text{O III}]\lambda 4363$  and the He II recombination line at  $4686 \text{ \AA}$  can rule out shocks as a dominant ionizing mechanism and point towards hot stars as the primary ionizing agent in the ISM. The indicator used to determine the presence/absence of shocks is given by the ratio between the  $[\text{O III}]\lambda 4363$  and the sum of  $\lambda 4959$  and  $5007$  lines, often called  $R_{\text{OIII}}$ .

Most shock models predict this ratio to be between 0.05–0.07, e.g. in Ref. [28]. Photoionization models predict smaller  $R_{\text{OIII}}$  values because the  $[\text{O III}]$ -emitting gas is cooler. At a temperature of 10 000 K,  $R_{\text{OIII}}$  is found to be about 0.005 in low density gas. We found that at the centre of Hydra A  $R_{\text{OIII}}$  does not fall into that above limit, which strongly indicates that shocks are not the dominant ionization process. Figure 5a illustrates the radial variation of the  $R_{\text{OIII}}$  ratio. The two values of the limits for the shocks models are illustrated by the dotted lines.

### 3.5 Helium recombination lines

We can measure the He II recombination line at  $4686 \text{ \AA}$  in our blue spectra. We can also estimate the He I recombination lines at  $4471 \text{ \AA}$  in blue and  $6678 \text{ \AA}$ ,  $5876 \text{ \AA}$  in red. He I line at  $6678 \text{ \AA}$  is very weak and blended by the  $[\text{S II}]$  doublet and  $[\text{N II}]\lambda 6583$ . He I line at  $5876 \text{ \AA}$  could not be used because of the contamination from the broad Na I absorption line. The most reliable measurement to be used in this case is  $I(4686)/I(\text{H}\beta)$ . Our results suggest that the He II recombination line is present in this galaxy. And its existence indicates that there is either very high energy photons or high energy particles ionizing gas near the nucleus than further out in the galaxy. In addition, the He II recombination line is not common around gases photoionized by hot stars – photon energies are not typically sufficient to get the He II recombination line or the 54 eV ionizing photons. It is possible that sufficiently energetic charged particles or X-rays are responsible for the collisional ionization. Figure 5b demonstrates the radial variation of the He II recombination line for Hydra A. The dotted line shows the zero value of the  $I(4686)/I(\text{H}\beta)$  ratio.

Figure 6 illustrates a typical fitting of the central bin of Hydra A with GANDALF, with black line representing the best fitting model spectra. The stellar component of this model is shown in the green line, whereas the best-fitting nebular spectrum is shown in red. The  $[\text{O III}]\lambda 4363$  and  $\text{He II}\lambda 4686$  lines are detected even though they are the weakest lines. The ratios between the Gaussian model amplitude and the level of noise in the residuals,  $A/N$ , which relate to the detection level of the two lines are closer to the limit of 2 (see the zoomed plot).



(a) Shocks using  $R_{\text{OIII}}$  ratio. Shocks models are limited by the dotted line (see text for details). (b) photoionization using  $I(4686)/I(\text{H}\beta)$  ratio. Dotted line shows the zero value of the ratio.

Figure 5: Model independent shocks and photoionization.

#### 4. Sources of ionization

In the previous section, we have used the model-independent method to investigate the sources of the ionization. We are now looking at the different photoionization models.

There are several possible sources of ionization of the hot gas in the cool-cores of galaxy clusters. The most popular ideas have been: (a) the central AGN, (b) young stellar populations, (c) X-rays from the ICM, (d) heat conduction from the ICM to the cold filament, (e) shocks and turbulent mixing layers, and (f) collisional heating by cosmic rays. In Figure 3 we show our line measurements with model predictions for shocks of various speeds and magnetic field strengths from [27]. The shock models cover the same range as our data in the  $[\text{N II}]/\text{H}\alpha$  and  $[\text{S II}]/\text{H}\alpha$  diagrams, but overpredict  $[\text{O I}]/\text{H}\alpha$ . These model grids match the centre of galaxy by slow shocks ( $v \sim 250\text{--}300 \text{ km s}^{-1}$ ) and its edge by much faster shocks ( $v \sim 300\text{--}500 \text{ km s}^{-1}$ ).

We show other ionization models compared to our data in Figure 7, 8 and 9. Figure 7 presents the model expectations for a dust-free AGN by [29], assuming a solar and twice solar metallicity and  $n_e$  of  $100 \text{ cm}^{-3}$ . The models with a twice solar metallicity accurately predict the  $[\text{N II}]/\text{H}\alpha$  ratios, but underpredict the  $[\text{S II}]/\text{H}\alpha$  and  $[\text{O I}]/\text{H}\alpha$  ratios. However, the models with a solar metallicity are the better fit to the data. We also measured the ionization parameter tracked by  $[\text{O II}]\lambda\lambda 3726, 3729$  and  $[\text{O III}]\lambda 5007$  in Figure 8. The models of photoionization by the dust-free AGN are the same as in [29]. The  $[\text{O II}]/[\text{O III}]$  ratios do change visibly from the centre of the AGN but there is no systematic trend. This could rule out the central AGN photoionization since the photoionization parameter should decrease as the observations move away from the centre i.e.  $[\text{O}$

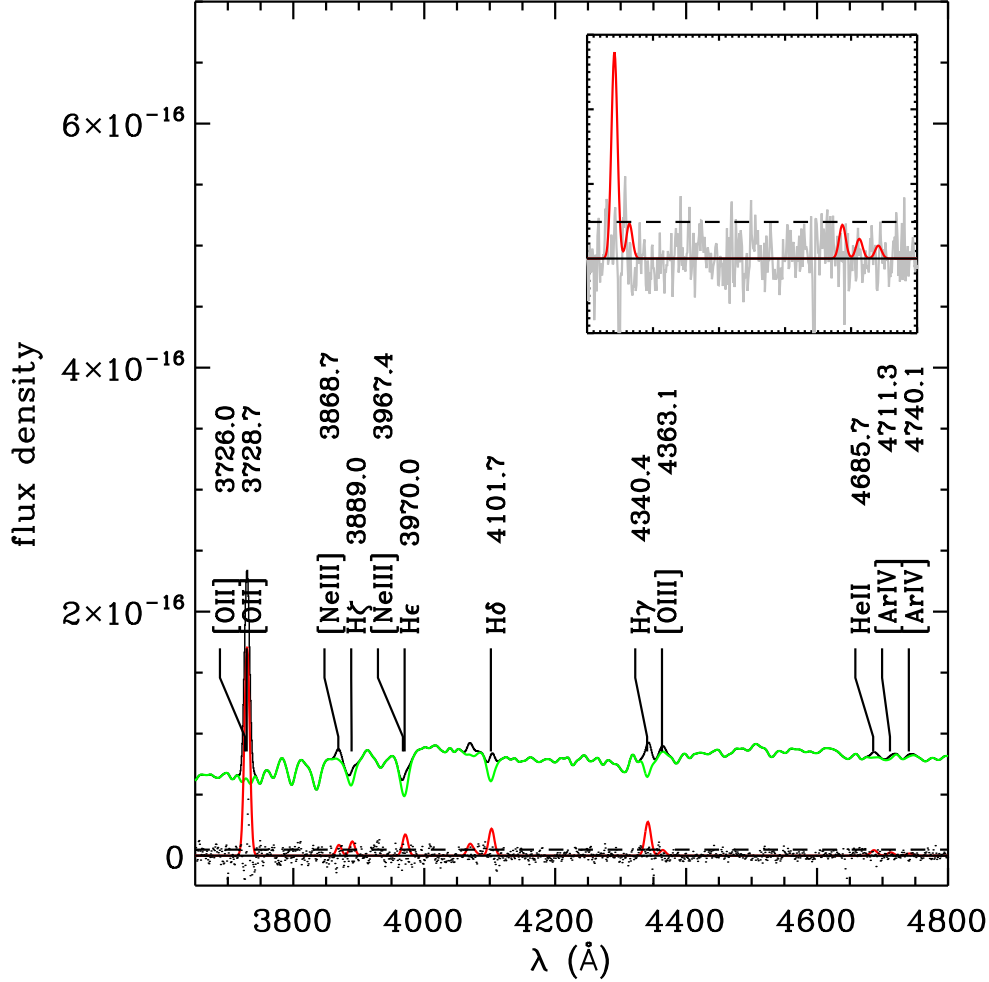


Figure 6: Example of the Gaussian fitting to the central bin of Hydra A in the region of [O III] $\lambda$ 4363 and He II recombination line at 4686 Å. The black line shows the best-fitting model spectrum is plotted in black line with highlights of the best-fitting emission lines. The green line indicates the best-fitting stellar component with the emission lines subtracted. The red line indicates the flux density for the measured emission lines. Residuals from the fit are also shown in the bottom panel with the dotted line. The dashed line shows the level of the amplitude-to-noise ratio in the residuals which corresponds to the detection level of the lines. The zoomed plot in the region of 4300–4800 Å shows the level of the A/N of both [O III] $\lambda$ 4363 and He II $\lambda$ 4686 lines and the residuals with grey line.

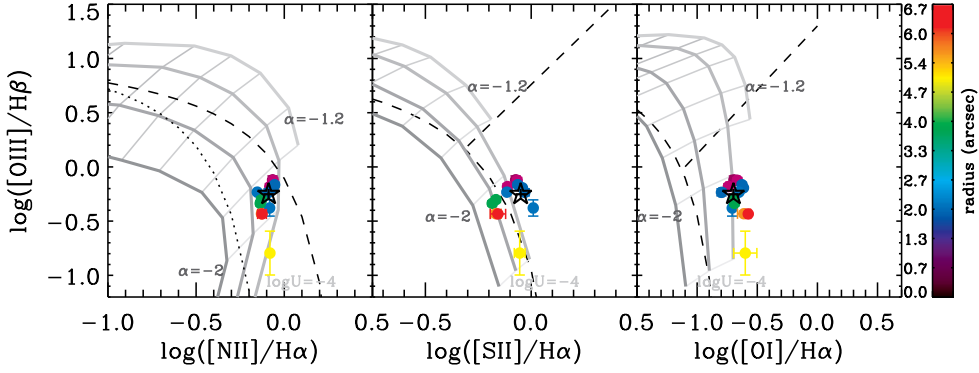


Figure 7: BPT diagrams with photoionization by a dust-free AGN model predictions overlaid. The models are for  $Z = 2Z_{\odot}$  (in the left plot) and  $Z = Z_{\odot}$  (in the middle and right plots), and  $n_e = 100 \text{ cm}^{-3}$ . The grids of photoionization is taken from [29]. From left to the right, the power-law spectral indices of  $\alpha = -2, -1.7, -1.4$  and  $-1.2$  are indicated by the curved lines. From top to the bottom, the lines represent the ionization parameter of  $\log U = -4, -3.3, -2.6, -2, -1.3, -0.60$  and  $0$ . The parameter increases with  $[\text{O III}]\lambda 5007/\text{H}\beta$ .

$\text{II}/[\text{O III}]$  ratios would increase when moving away from the AGN. The AGN is thus not radiatively dominating the ionization of the filaments, if it contributes at all. The ratios were measured using the blue spectra since both O II and O III emission lines are in blue. It is preferable to measure those ratios from the same spectra.

The first panel demonstrated by hexagons in Figure 9 is the model predictions for collisional ionization by cosmic rays [30]. These models produce very low  $[\text{O III}]/\text{H}\beta$  ratios. The second panel represented by the opened triangles is the photoionization by the hot X-ray [31]. The model predictions are in good agreement with the observed line ratios on the  $[\text{S II}]/\text{H}\alpha$  and  $[\text{O I}]/\text{H}\alpha$  diagrams. The consistency with the observed data is not surprising given the star formation present in this system. However,  $[\text{N II}]/\text{H}\alpha$  ratios are slightly overpredicted by the models. The third panel is the model expectations for the heat conduction along the boundary between the hot ICM and the cool filaments from [32]. These models also fail to produce the observed ratios. Thus, neither cosmic rays nor conduction can be the dominant source of ionization in Hydra A. It is likely, however, that a combination of shocks, photoionization by hot X-ray and AGN is responsible for heating the gas (see model-independent results in sections 3.4 and 3.5).

## 5. Conclusion

We present SALT and Gemini data for Hydra A, as part of a larger project to study eight star forming BCGs in detail, for which data has been collected on SALT during a two year period. This data enables us to measure all the emission lines (with  $A/N > 2$ ) in the optical wavelength range. Our initial calculations of the hot gas properties illustrate a variety of gas kinematics and ionization mechanisms as well as a change in hot gas properties further from the galaxy nucleus. Here, we have presented some preliminary results of Hydra A from using the model independent measurements and photoionization models from the literature in the form of the BPT diagrams.

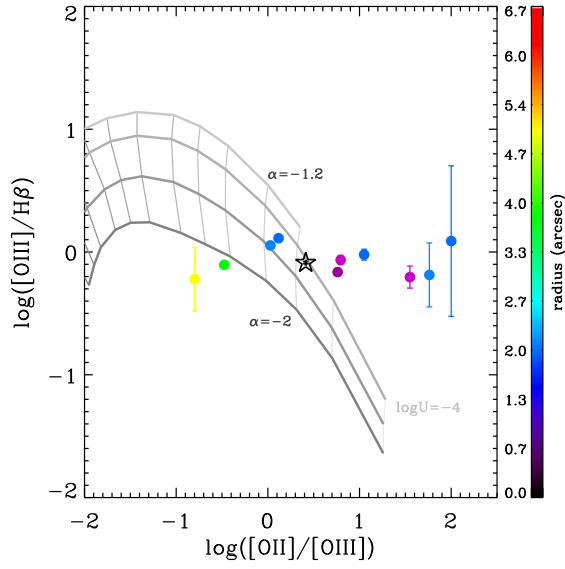


Figure 8:  $[\text{O III}]\lambda\lambda 3726,3729/[\text{O III}]\lambda 5007$  vs  $[\text{O III}]\lambda 5007/H\beta$ . The photoionization by a dust-free AGN model was taken from [29], computed with the same parameters as in the left plot of the previous figure.

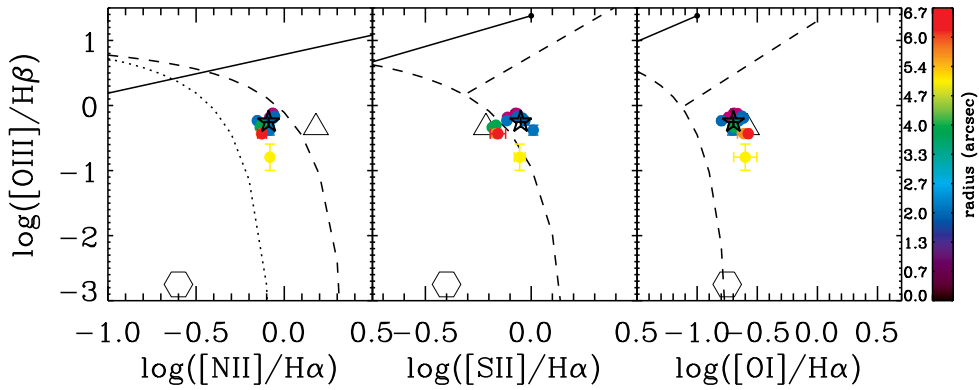


Figure 9: BPT diagrams with conduction, X-ray heating and cosmic rays model predictions overlaid. The collisional ionization by cosmic rays predictions are indicated by hexagon symbols (using model predictions by [30]). The photoionization by the hot X-ray heating models from [31] are shown in open triangle. The conduction lines (black solid lines) are from [32] and correspond to different initial conditions.

Both methods show that a combination of sources of ionization was found to heat the gas in this BCG, that includes shocks, photoionization by hot X-ray and AGN.

Placing the hot gas ionization mechanisms into context with all available data from X-ray (ICM) through radio should allow for more insight into the cooling–feedback cycle, while combining the hot gas kinematics with deep X-ray and radio studies may shed new light on the motion of this gas.

## Acknowledgements

ALR and SIL are financially supported by the South African National Research Foundation. All of the observations reported in this paper were obtained with SALT under program 2013-1-RSA\_OTH-011, 2013-2-RSA\_OTH-002, 2014-1-RSA\_OTH-003, 2014-2-SCI-014 (PI: Ilani Loubser).

## References

- [1] Bildfell C., Hoekstra H., Babul A., Mahdavi A. 2008 *MNRAS* **389** 1637
- [2] Pipino A., Kaviraj S., Bildfell C., Babul A., Hoekstra H., Silk J. 2009 *MNRAS* **395** 462
- [3] Best P. N., von der Linden A., Kauffmann G., Heckman T. M., Kaiser C. R. 2007 *MNRAS* **379** 894
- [4] Loubser S. I., Soechting I. K. 2013 *MNRAS* **431** 2933
- [5] Rafferty D. A., McNamara B. R., Nulsen P. E. J. 2008 *ApJ* **687** 899-918
- [6] Quillen A. C., et al. 2008 *ApJS* **176** 39-58
- [7] Edge A. C., et al. 2002 *MNRAS* **337** 49
- [8] Loubser S. I., et al. 2016 *MNRAS* **456** 1565
- [9] von der Linden A., Best P. N., Kauffmann G., White S. D. M. 2007 *MNRAS* **379** 867
- [10] Binette L., Dopita M. A., Tuohy I. R. 1985 *ApJ* **297** 476
- [11] Donahue M., Voit G. M. 1991 *ApJ* **381** 361
- [12] Voit G. M., Donahue M. 2015 *ApJ* **799** L1
- [13] McCourt M., Sharma P., Quataert E., Parrish I. J. 2012 *MNRAS* **419** 3319
- [14] Gaspari M., Ruszkowski M., Sharma P. 2012 *ApJ* **746** 94
- [15] Voit G. M., Donahue M., Bryan G. L., McDonald M. 2015 *Natur* **519** 203
- [16] Voit G. M., Meece G., Li Y., O’Shea B. W., Bryan G. L., Donahue M., 2016 [arXiv:1607.02212]
- [17] Edwards L. O. V., Robert C., Mollá M., McGee S. L. 2009 *MNRAS* **396** 1953
- [18] Donahue M., et al. 2010 *ApJ* **715** 881
- [19] S. I. Loubser , A. Ratsimbazafy, in proceedings of *SALT Science Conference PoS(SSC2015)015*
- [20] Sarzi M., et al., 2006, *MNRAS*, 366, 1151
- [21] Calzetti D., Armus L., Bohlin R. C., Kinney A. L., Koornneef J., Storchi-Bergmann T. 2000 *ApJ* **533** 682
- [22] Baldwin J. A., Phillips M. M., Terlevich R. 1981 *PASP* **93** 5
- [23] Kewley L. J., Dopita M. A., Sutherland R. S., Heisler C. A., Trevena J. 2001 *ApJ* **556** 121
- [24] Kauffmann G., et al. 2003 *MNRAS* **346** 1055
- [25] Heckman T. M., Baum S. A., van Breugel W. J. M., McCarthy P. 1989 *ApJ* **338** 48
- [26] De Robertis M. M., Dufour R. J., Hunt R. W. 1987 *JRASC* **81** 195
- [27] Allen M. G., Groves B. A., Dopita M. A., Sutherland R. S., Kewley L. J. 2008 *ApJS* **178** 20-55

- [28] Dopita M. A., Sutherland R. S. 1996 *ApJS* **102** 161
- [29] Groves B. A., Dopita M. A., Sutherland R. S. 2004 *ApJS* **153** 75
- [30] Ferland G. J., et al. 2009 *MNRAS* **392** 1475
- [31] ] Voit G. M., Donahue M., 1990 *ApJ* **360** L15
- [32] Boehringer H., Fabian A. C. 1989 *MNRAS* **237** 1147